Available online at www.sciencedirect.com

ScienceDirect

Geochimica et Cosmochimica Acta 333 (2022) 166–183

Geochimica et Cosmochimica Acta

www.elsevier.com/locate/gca

Heavy $\delta^{26}Mg$ values in carbonate indicate a magmatic-hydrothermal origin of Carlin-type Au deposit

Zhuojun Xie [a,*], Kang-Jun Huang [b], Yong Xia [a,*], Jean Cline [c], Qinping Tan [a], Jianzhong Liu [d,e], Jingdan Xiao [a,f], Bing Yan [a,f]

[a] State Key Laboratory of Ore Deposit Geochemistry, Institute of Geochemistry, Chinese Academy of Sciences, Guiyang 550081, China
[b] State Key Laboratory of Continental Dynamics, Shaanxi Key Laboratory of Early Life and Environments, Department of Geology, Northwest University, Xi'an 710069, China
[c] University of Nevada Las Vegas, Las Vegas, NV 89154, USA
[d] Technology Innovation Center of Mineral Resources Explorations in Bedrock Zones, Ministry of Natural Resources of People's Republic of China, Guiyang 550081, China
[e] Guizhou Bureau of Geology and Mineral Exploration & Development, Guiyang 550018, China
[f] University of Chinese Academy of Sciences, Beijing 100039, China

Received 12 May 2022; accepted in revised form 6 July 2022; available online 11 July 2022

Abstract

The Carlin-type Au deposits in Youjiang Basin, SW China, (referred to as Guizhou Carlin-type Au deposits) are the second largest Carlin-type Au province in the world after Nevada, USA. To date, the source of ore fluids that formed the Guizhou deposits remains controversial, hampering the formulation of a genetic model. Compared to Nevada Carlin-type Au deposits, a significant difference is that the Guizhou Carlin-type Au deposits contain abundant ore-stage dolomite in the ore. Herein, we present carbonate Mg isotopes combined with C-O isotopes from the giant Shuiyindong deposit to provide new insights into the source of ore fluids and to constrain the ore genesis of the Guizhou Carlin-type Au deposits.

Petrographic observation shows that from least altered bioclastic limestone to high-grade ore, dolomite increased significantly, suggesting that dolomite formed as part of the Au mineralization process. Chemical analyses reflect a small amount of Mg in the ore fluids was variably added to ore during Au mineralization, and this added Mg was fixed in the dolomite. Although most ore-stage dolomite formed from the sulfidation of Fe in Fe-dolomite, some ore-stage dolomite formed by the combination of host rock calcite with Mg from ore fluids.

The $\delta^{26}Mg$ values of carbonate, primarily dolomite, range from −3.49‰ to −0.07‰, with a median value of −1.01‰. The $\delta^{18}O$ values range from 21.7‰ to 27.6‰, with a median value of 23.2‰. The $\delta^{13}C$ values vary from −14.6‰ to 1.2‰, with a median value of −0.7‰. The $\delta^{26}Mg$ values exhibit a positive correlation trend with MgO, S, SiO_2, and Carlin-suite elements (Au, As, Hg, Sb, Tl, and Cu), and a negative correlation trend with CaO. Comparison of Mg isotopes data from this study with the major Mg reservoirs indicates that the Shuiyindong samples contain heavier Mg isotopes that drifts towards the heavy Mg reservoirs (magmatic and metamorphic rocks) compared with normal carbonate rocks. Two mechanisms, namely heavy Mg addition from ore fluids and isotopic exchange reaction with heavy Mg-rich ore fluids, could have attributed to heavy Mg in carbonates in the Shuiyindong deposit.

The Mg isotopes results, combined with other isotopes (e.g., S, Hg, and He-Ar) and geologic evidence, support a magmatic-hydrothermal origin for the ore fluids. The thick Devonian-Triassic sedimentary sequence and weak extension following sedimentation prevented igneous activity from reaching the surface. However, buoyant ore fluids released from the deep-seated intrusions are interpreted to have ascended along basement-penetrating faults and eventually produced the

* Corresponding authors.
E-mail addresses: xiezhuojun@mail.gyig.ac.cn (Z. Xie), xiayong@mail.gyig.ac.cn (Y. Xia).

https://doi.org/10.1016/j.gca.2022.07.009

Guizhou Carlin-type Au deposits at shallow levels. This study implies that Mg isotopes are a novel proxy to infer ore fluids source and evolution, and that they can provide significant constraints on the genesis of hydrothermal deposit.

Keywords: Carlin-type Au deposit; Magmatic-hydrothermal origin; Gold deposit; Magnesium (Mg) isotope; Hydrothermal dolomite

1. INTRODUCTION

Carlin-type Au deposits, accounting for ~ 6% of annual worldwide Au production, are mainly located in Nevada, USA, and the Dian-Qian-Gui area, southwest China (Hofstra and Cline, 2000; Cline et al., 2005; Muntean and Cline, 2018; Xie et al., 2018a). The Nevada Carlin-type Au deposits with an Au endowment of 7930 tons are the second largest concentration of Au in the world after deposits in South Africa (Muntean and Cline, 2018). The Au deposits in the Dian-Qian-Gui area, southwest China, (from here on referred to as Guizhou Carlin-type Au deposits) have an Au endowment of ~ 900 tons (Liu et al., 2020). Recent exploration and studies indicate that the Nevada Carlin-type Au deposits are temporally and spatially related to the south-southwest sweep of magmatism that resulted from the rollback/removal of the Farallon plate, and the deposits are suggested to have formed from the magmatic-hydrothermal fluids released at depths of ~ 10–12 km (Kesler, et al., 2005; Ressel and Henry, 2006; Muntean et al., 2011; Large et al., 2016; Mercer, 2021). For the Guizhou Carlin-type Au deposits, a relationship with magmatism has been controversial because of a lack of magmatic activity that is spatially and temporally associated with the deposits. Previous studies of the Guizhou deposits resulted in two end-member models regarding the sources of ore fluids: (1) circulation of shallow fluids including meteoric water or basin fluid mobilized ore-forming elements from sedimentary strata to form the deposits (Liu et al., 2001; Wang et al., 2002; Hu et al., 2017); (2) ore fluids liberated by deep magmatism or metamorphic dehydration ascended to shallow levels and precipitated metals in sedimentary rocks (Su et al., 2009; 2018; Xie et al., 2018b; Jin et al., 2020; Zhu et al., 2020).

Compared to Nevada Carlin-type Au deposits, one of the most significant differences for Guizhou deposits is that they exhibit dolomite-stable alteration (Xie et al., 2017; 2018a). The widespread occurrence of dolomite in Guizhou ore and its intergrowth with Au-bearing pyrite suggests that the dolomite precipitated during the main-ore stage (Xie et al., 2017; 2018a; Su et al., 2018). Thus, dolomite chemistry and isotopic compositions can provide constraints on the genesis of the deposits.

Magnesium (Mg) is a major element in dolomite. Mg isotopes have a large variation (>7‰) in nature, and different reservoirs have distinguishing δ^{26}Mg values (Teng, 2017). Igneous rocks commonly have a limited variability of Mg isotopic composition, with δ^{26}Mg values ranging mainly from −0.4‰ to 0‰ (Li et al., 2010; Teng et al., 2010; Huang et al., 2016, and references therein; Teng, 2017). Metamorphic rocks and siliciclastic sedimentary rocks have δ^{26}Mg values similar to the igneous rocks, and the metamorphic rocks have a relatively broader variation of δ^{26}Mg compared with the igneous rocks (Teng, 2017 and references therein). Alternatively, the carbonate rocks have remarkably low and variable δ^{26}Mg values, ranging mainly from −5‰ to −1‰, significantly different from the igneous rocks (Teng, 2017 and references therein).

Mg isotopes are significantly fractionated during low-temperature geological processes and are fractionated less during high-temperature geological processes (Teng, 2017). Chemical weathering (fluid-rock interaction) can induce large Mg isotopic fractionation, resulting in light Mg released into water and leaving heavy Mg in the residue (Galy et al., 2002; Young and Galy, 2004; Tipper et al., 2006, 2012; Huang et al., 2012; Li et al., 2014; Teng, 2017). Magmatic processes, including partial melting, magmatic differentiation, and fractional crystallization, exhibit a limited Mg isotopic fractionation, although small inter-mineral isotopic fractionation was observed in high temperature rocks (Teng et al., 2010; Liu et al., 2010; Li et al., 2011; Wang et al., 2016; Teng, 2017, and reference therein). Although the Mg isotopic fractionation during fluid exsolution from magma has not been well constrained, fluid exsolution should not induce significant Mg isotopic fractionation because (1) Mg isotopic fractionation is limited to high-temperature processes (Teng, 2017); and (2) Mg isotopes exhibit fractionation behavior similar to Fe isotopes, and a recent study demonstrated that Fe isotopes show limited fractionation during fluid exsolution (Du et al., 2019). Additionally, metamorphism process also exhibits a limited Mg isotopic fractionation (Li et al., 2011; 2014; Wang et al., 2014). The larger variation of Mg isotopes in different reservoirs and the well constrained fractionation behavior of Mg isotopes during major geological processes make Mg isotopes a potential tracer to constrain sources and the evolution of the Mg-rich ore fluids.

In this contribution, we present an integrated study of carbonate Mg, C and O isotopes, and whole rock major and trace elements compositions from the giant Shuiyindong deposit, southwestern Guizhou Province, China. These new results, particularly the heavy Mg isotopic composition of carbonates, suggest that the Guizhou Carlin-type Au deposits formed from deep rather than shallow ore fluids, which were most likely released from the deep-seated intrusions.

2. GEOLOGICAL BACKGROUND

2.1. Regional geology

Almost all Guizhou Carlin-type Au deposits are tectonically formed in the Youjiang Basin (Fig. 1). The diamond-shaped basin is situated on the southwestern margin of the

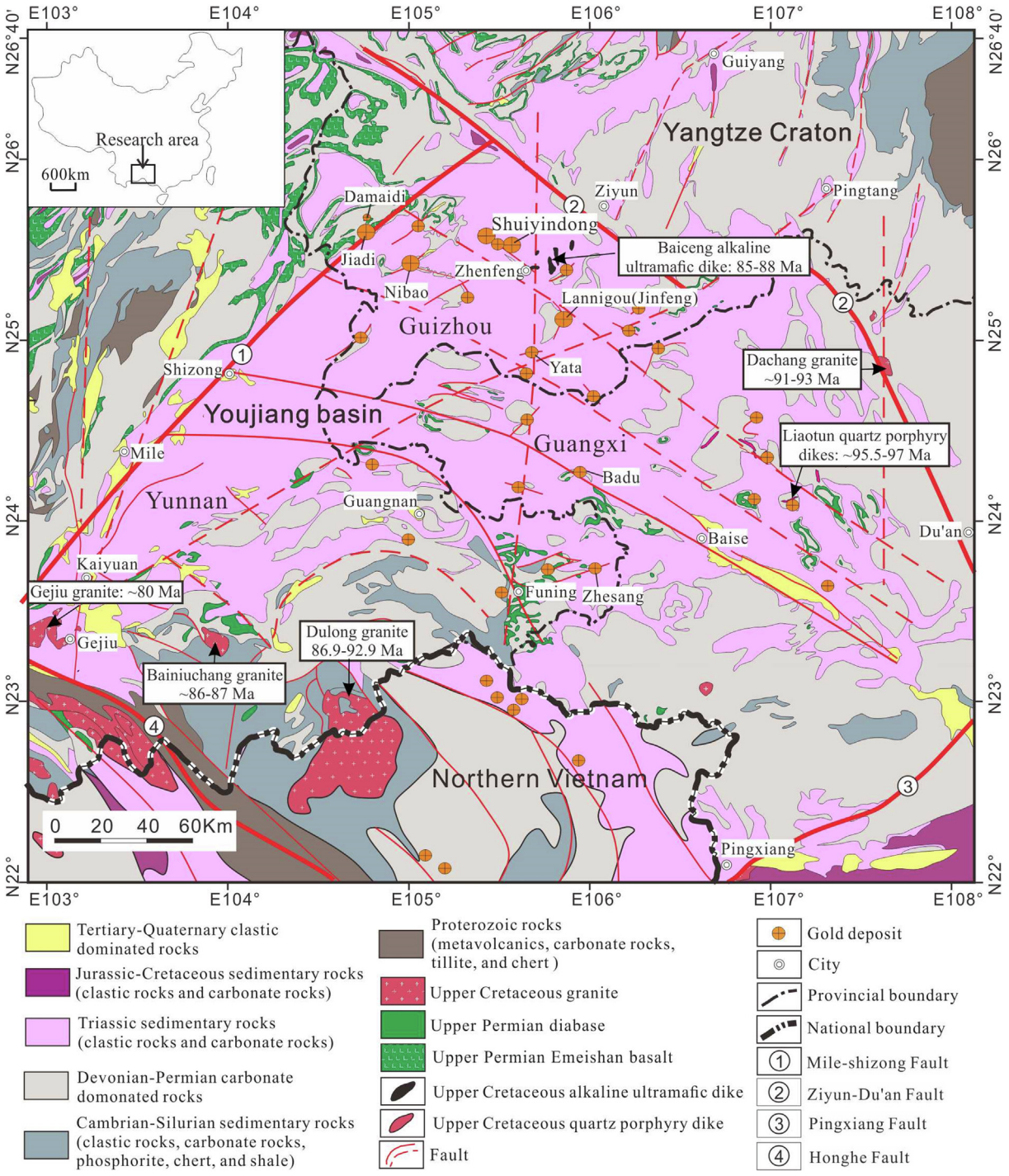

Fig. 1. Regional geologic map showing the distribution of Carlin-type Au deposits in the Youjiang basin (modified from Su et al., 2018; Li et al., 2021).

Yangtze craton, separated from the Indochina block by the Red River fault to the southwest, from the Cathaysia block by the Pingxiang fault to the southeast, and bounded by the Ziyun-Du'an fault and the Mile-Shizong fault in the northeast and northwest, respectively (Fig. 1). The evolution of the Youjiang Basin was summarized by Xie et al. (2018a) and Su et al. (2018) and is briefly described here. The basin was initiated by early Devonian passive-margin rifting along the southwestern margin of the Precambrian Yangtze craton (Xie et al., 2018a; Su et al., 2018). The rifting event produced a series of NW- and NE-striking high-angle basement-penetrating normal faults that subsequently con-

trolled sedimentation, deformation, and magmatism (Xie et al., 2018a; Su et al., 2018). Subsequent to rifting from the early Devonian to early Triassic, sedimentation within the basin was dominated by shallow-water platform-facies carbonate rocks. From the middle to late Triassic (or early Jurassic) in the northwestern part of the basin, a sequence of platform-facies sedimentary rocks mainly consisting of carbonate rocks interbedded with detrital rocks was deposited. Alternatively, in the southern and eastern part of the basin, deeper-water slope/basin-facies sedimentary rocks dominated by fine-grained clastic rocks interbedded with thinly layered carbonate rock and sandstone developed. The late Permian and Triassic sedimentary sequences host most Carlin-type Au deposits in the basin (Xie et al., 2018a; Su et al., 2018).

Tectonically, the Youjiang Basin is located at the transitional area between the Tethyan and Pacific tectonic domains, and two tectonic episodes may have influenced the magmatism and deformation of the basin. Li and Li (2007) proposed that the west-verging subduction of the Pacific plate beneath Eurasian began to flatten at ~ 250 Ma, and this slab began to break off at ~ 190 Ma. Slab breakoff and rollback resulted in a transition from contractional deformation to extension and the initiation of intensive granitic intrusion and felsic volcanism in eastern China, about 300–600 km east of the Carlin-type Au deposits in the basin (Li and Li, 2007). Alternatively, the southwest-verging subduction of Ailaoshan-Song Ma branch of the Paleo-Tethys Ocean beneath the Indochina block during the early Permian resulted in the formation of arc magmatism along the Truong Son fold belt in Vietnam (Zaw et al., 2014). Slab-pull extension driven by this subduction may have reopened the basement structures and led to the formation of late Permian diabase intrusions in the basin (Su et al., 2018). During the late Permian to middle Triassic, continued subduction resulted in the collision of Indochina with South China (Indosinian orogeny), which caused the emplacement of Triassic syncollisional granites and metamorphism along the border between Vietnam and Yunnan (Zaw et al., 2014; Su et al., 2018). The late Triassic to early Jurassic Indochina-Sibumasu collision (Yanshanian orogeny) led to intracontinental deformation of the basin. Following the northeast-verging subduction of the Meso-Tethys Ocean beneath Sibumasu during the Cretaceous (Zaw et al., 2014), extension may have caused emplacement of the late Cretaceous granites (~80–96 Ma), quartz porphyry dikes (95–97 Ma), and alkaline ultramafic dikes (85–88 Ma) in the basin (Fig. 1). Some of these granitic intrusions contributed to the formation of polymetallic tin/tungsten deposits, but they are not spatially associated with the Carlin-type Au deposits (Fig. 1). Most of the dikes are ~ 10 to 30 km from the Carlin-type Au deposits (Fig. 1). There is only one unaltered quartz porphyry dike (95.5 ± 0.7 Ma) that crosscuts a mineralized fault at the Liaotun Au deposit (Chen et al., 2014).

The timing of Guizhou Carlin-type Au mineralization is still not well constrained because of a lack of minerals clearly associated with Au deposition that are suitable for isotopic dating. Su et al. (2018) and Xie et al. (2018a) discussed ages proposed for Au mineralization using different methods and concluded that most reliable proposed ages are based on cross-cutting relationships, indicating that the Au deposits in the northern margin of the basin may have formed between Jurassic and late Cretaceous time.

Recent advances of analytical techniques and methods [e.g., secondary ion mass spectrometry (SIMS), and laser ablation-multicollector-inductively coupled plasma-mass spectrometry (LA-MC-ICP-MS)] allow for in situ dating of hydrothermal minerals. Pi et al. (2017) dated hydrothermal rutile associated with Au-bearing sulfides in the Zhesang deposit using SIMS U-Pb, and results yielded ages of 213.6 ± 5.4 Ma. Chen et al. (2019) obtained a mean Th-Pb age of 141 ± 3 Ma for apatite coeval with auriferous pyrite from the Nibao deposit using SIMS. Gao et al. (2021) dated the hydrothermal rutile and monazite associated with ore-stage pyrite from the Badu deposit using SIMS U-Th-Pb, and results yielded ages of 141.7 ± 5.8 M a and 143.5 ± 1.4 Ma, respectively. Jin et al. (2021) determined U-Pb ages of 204.3 ± 2.0 to 202.6 ± 2.5 Ma, 191.9 ± 2.2 Ma, and 139.3 ± 5.7 to 137.1 ± 9.7 Ma for three stages of calcite that are associated with Au mineralization from the Shuiyindong deposit using LA-ICP-MS and LA-MC-ICP-MS. Collectively, these dating results suggest that the Au deposits in the Youjiang Basin may have formed from two different mineralization events (Hu et al., 2017; Su et al., 2018). The deposits in the southern margin of the basin could have formed in the middle-late Triassic (232–212 Ma), whereas the deposits in the northern margin could have primarily formed in the late Jurassic-early Cretaceous (148–134 Ma) (Su et al., 2018).

2.2. Geology of Shuiyindong deposit

The Shuiyindong deposit, located in the north of Youjiang Basin (Fig. 1), is the largest Carlin-type Au deposit in China with proven and probable Au reserves of 290 tonnes and an average Au grade of 5 g/t (Liu et al., 2017). The deposit consists of four ore blocks including Shuiyindong, Xionghuangyan, Bojitian, and Nayang (Fig. 2). The geology of the Shuiyindong deposit was described in detail by Xie et al. (2018a) and Su et al. (2018) and is briefly summarized here.

Sedimentary strata in the deposit area consist of the middle Permian Maokou, upper Permian Longtan, Changxing, and Dalong, and lower Triassic Yelang and Yongningzhen Formations (Figs. 2, 3B). Igneous rocks are absent in the deposit district. The Baiceng alkaline ultramafic dikes, ~20 km from the deposit, are the nearest igneous rocks (Fig. 1). However, Bouguer gravity and magnetic surveys indicate a pluton ~ 5 km below the surface at Shuiyindong (Liu et al., 2017).

The deposit is controlled by the nearly E-trending Huijiabao anticline, which is ~ 5 km wide and ~ 20 km long and plunges eastward. The north and south limbs dip at low angles and are cut by the reverse faults F101 and F105, respectively (Fig. 2). A series of near NS-trending normal faults cut the two reverse faults (Fig. 2). The Lanmuchang Hg-Tl-Au deposit, located a few kilometers to the southwest of the Shuiyindong deposit, is controlled by these normal faults (Fig. 2).

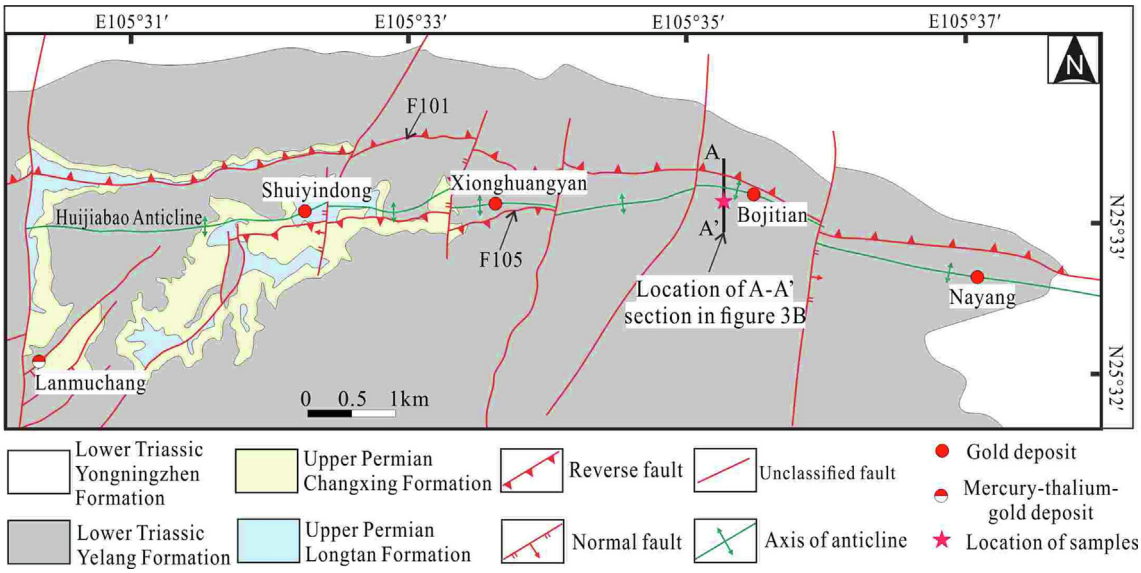

Fig. 2. Geologic map showing the sedimentary strata and main structures of the Shuiyindong deposit, which includes the Shuiyindong, Xionghuangyan, Bojitian, and Nayang ore blocks. Line B-B' marks the location of the cross section shown in Fig. 3b (modified from Tan et al., 2015; Xie et al., 2018a).

Gold mineralization mainly occurs in the crest and flanks of the Huijiabao anticline and is preferentially disseminated in bioclastic limestone of the second and third units of Longtan Formation, along with a minor ore body hosted in the Changxing, Dalong, and Yelang Formations (Fig. 3B). The strata above and below the bioclastic limestone orebodies are typically thick-bedded argillite. An unconformity between the Longtan and underlying Maokou Formations (SBT) also hosts some low-grade strata-bound orebodies (Fig. 3B). This unconformity was identified as the regional structural conduit that fed ore fluids into the upper strata (Tan et al., 2015; Liu et al., 2020).

Gold occurs primarily as ionic Au in arsenian pyrite, with minor Au in arsenopyrite (Liang et al., 2021). The arsenian pyrite is enriched in Cu, Sb, Hg, and Tl in addition to Au and formed by the sulfidation of Fe-rich carbonate rocks (Su et al., 2012; Xie et al., 2018a, 2018b; Li et al., 2020a). Hydrothermal alteration associated with auriferous pyrite precipitation includes both dissolution and silicification of calcite, formation of dolomite, and argillization of silicate minerals to form illite (Su et al., 2009; Xie et al., 2018a). These minerals were produced predominantly by fluid-rock reaction during the main-ore stage and are disseminated in ore. The late-ore stage minerals including orpiment, realgar, quartz, calcite, and stibnite precipitated in open space (Xie et al., 2018a; Su et al., 2009; 2018). Fluid inclusions studies indicate the deposit formed from ~ 220 to 345 °C aqueous fluids with low salinities (0.9–2.3 wt% NaCl equiv) and high CO_2 content (6.3–8.4 mol%) (Su et al., 2009). Additionally, individual fluid inclusion analyses using LA-ICP-MS reflect that ore-stage fluids contained up to 200 ppm Mg. However, Mg in the late-ore-stage fluids was below the detection limit (Su et al., 2009).

3. SAMPLING AND ANALYTICAL METHODS

3.1. Sampling

Fig. 3B documents the sampling locations. In this study, we selected a representative N-S cross section across the Huijiabao anticline for sampling and mainly focused on the bioclastic limestone layers. A total of 26 limestone (ore) samples were collected from 8 drilling holes, with 24 samples from three layers, including the second unit of Longtan and Changxing Formations and the first unit of Yelang Formation, and 2 samples from the high-grade ore in the third unit of Longtan Formation.

3.2. Whole rock major and trace element analyses

Whole rock major and trace element analyses (excluding Au and Hg) were performed at the Institute of Geochemistry, Chinese Academy of Sciences (IGCAS). The samples were cleaned with water, dried, and then powdered for analysis.

Major element analyses were determined using a Fusion X-ray Fluorescence Spectrometry (FU-XRF) method. SiO_2, Al_2O_3, Fe_2O_3, MgO, CaO, Na_2O, K_2O, MnO, P_2O_5, TiO_2, S were measured using an ARL Perform' X 4200 X-ray Fluorescence Spectrometer (XRF). Analyses of standards GBW07125 and GBW07108 are in good agreement with certified values, and Relative Standard Deviation (RSD) was typically better than 3% for all elements. Loss on ignition (LOI) was obtained using about 1 g of sample powder heated and kept temperature at 1100 °C for 3 h. Total C was analyzed using a combustion method. About 25–30 mg of sample powder were loaded into tin capsules, heated to 1050 °C, and then analyzed using an elemental analyzer (Elementar-vario MACRO).

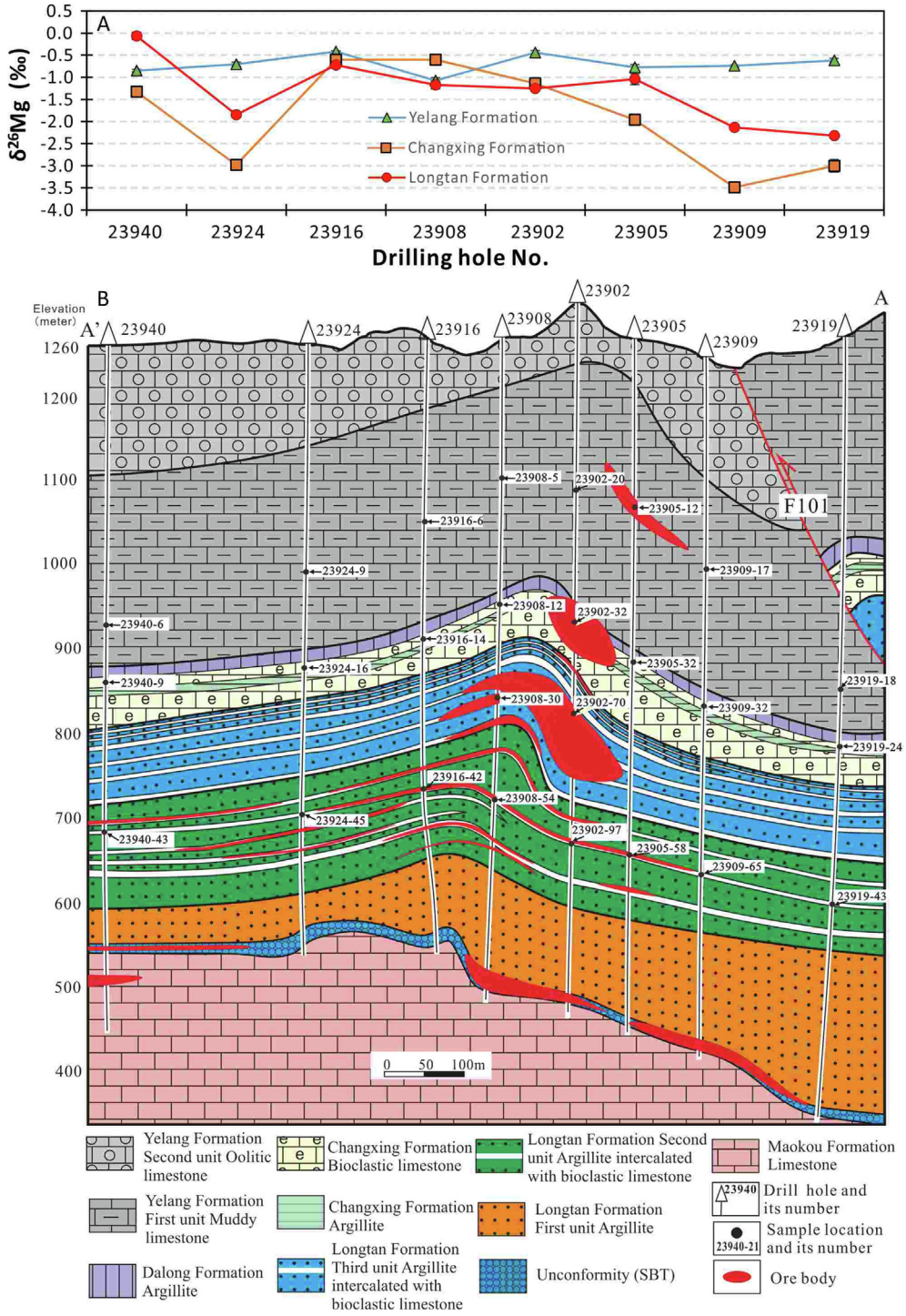

Fig. 3. Geological cross section of the Shuiyindong deposit showing mineralized Huijiabao anticline (B), sampling location (B), and the corresponding δ^{26}Mg value of carbonate fraction in bulk sample (A).

Trace element analyses were determined using a Plasma-Quant MS Elite Inductively Coupled Plasma Mass Spectrometry (ICP-MS). The analytical procedure was described in detail by Qi et al. (2000). About 50 mg of sample powder were dissolved in a high-pressure Teflon bomb using a HF + HNO_3 mixture heated to 185 °C for 32 h. Rhodium was used as an internal standard to correct for matrix effects and instrument drift. Concentrations of 47 elements including Li, Be, Sc, V, Cr, Co, Ni, Cu, Zn, Ga, Ge, As, Rb, Sr, Y, Zr, Nb, Mo, Ag, Cd, In, Sn, Sb, Cs, Ba, Hf, Ta, W, Tl, Pb, Bi, Th, U, and 14 of the rare earth elements, were measured for each sample. Analyses of

international standards OU-6 and GBPG-1 are in good agreement with certified values, and RSD was generally better than 10% for most elements.

Gold and Hg were analyzed at the Rock and Mineral Analysis Center, Henan Province, China. The analytical procedure was described in detail by Zhang et al. (2012). Gold and Hg was analyzed using an Atomic Absorption Spectrometry (AAS) and Cold Vapor-Atomic Fluorescence Spectrometry (CV-AFS) method, respectively. Concentrations of Au and Hg were measured by a XSERIES 2 ICP-MS and AFS-8330 Atomic Fluorescence Spectrophotometer, respectively. Analyses of standards are in good agreement with recommended values, and RSD was typically better than 40% for both Au and Hg. Detection limits for Au and Hg are about 0.1 ppb and 0.5 ppb, respectively (Zhang et al., 2012).

3.3. Carbonate C-O isotopes analysis

Carbon ($\delta^{13}C$) and O ($\delta^{18}O$) isotope ratios of bulk carbonates in samples were determined at the IGCAS. About 200–300 ug of sample powder were reacted with anhydrous H_3PO_4 at 72 °C to generate CO_2. Liberated CO_2 was purified by passage through liquid nitrogen cold traps in the Kiel IV carbonate device, and then introduced into a MAT 253 isotope ratio mass spectrometer for C and O isotopic measurements. Isotopic results are expressed in the standard δ notation as per mil (‰) deviation from Vienna PeeDee Belemnite (VPDB). Precision monitored by two international (IAEA-603 and IAEA-CO-8) and two Chinese (GBW04405 and GBW04416) standards is better than 0.1‰ and 0.2‰ for $\delta^{13}C$ and $\delta^{18}O$, respectively.

3.4. Carbonate Mg isotopes analysis

Mg isotope ratios for carbonate fractions in bulk samples were analyzed at the State Key Laboratory of Continental Dynamics, Northwest University, Xi'an, China. Chemical separation of the Mg fraction for isotopic analysis was performed using an established procedure (Geske et al., 2015; Huang et al., 2015; Li et al., 2016; Peng et al., 2016; Bao et al. 2019). About 10 mg of bulk sample powder was weighed and digested using 15 ml 0.5 N acetic acid in a centrifuge tube. The tube was placed in an ultrasonic bath for about 3 h at room temperature to allow complete dissolution of carbonate component. After centrifugation, supernatant was prepared for Mg isotopes analyses. About 25 μg Mg was obtained for chemical purification. Mg was purified by cation exchange chromatography, and two columns were used to separate Mg from other matrix metals. Mg recovery of the column chemistry was > 95%, and the matrix elements were < 1% of Mg after purification.

Mg isotope ratios were measured by a Nu Plasma II MC-ICP-MS using the sample-standard bracketing method. Analyses were performed in low-resolution and wet plasma mode, with ^{24}Mg, ^{25}Mg, and ^{26}Mg measured simultaneously in separate Faraday cups (L5, Ax, and H5). All samples were analyzed three times within an analytical session. Results are reported in the δ notation as per mil (‰) deviation relative to the DSM3 standard: $\delta^{X}Mg = [(^{X}Mg/^{24}Mg)_{sample} / (^{X}Mg/^{24}Mg)_{DSM} - 1]*1000$, where X = 25 or 26. The internal precision during a single analytical session is better than ~ ±0.10‰ (2SD). The external precision was determined by measurements of two USGS standards (BCR-2 and BHVO-2) and seawater standards. The long external precision is better than ~±0.06‰ (2SD). The BCR-2, BHVO-2, and seawater standards have average $\delta^{26}Mg$ of −0.19 ± 0.03‰, −0.14 ± 0.03‰, and −0.89 ± 0.03‰, respectively, matching the published values (Huang et al., 2018).

4. RESULTS

4.1. Petrography and mineralogy

Bioclastic limestone is the major host rock in the Shuiyindong deposit. Least altered (Au < 0.01 g/t) bioclastic limestone contains abundant bioclasts which are mainly composted of calcite, with minor Fe-dolomite and quartz (Fig. 4A-B). Pure dolomite was rarely observed in barren and low-grade samples. Trace kaolinite is occasionally observed in low-grade samples.

High-grade (Au > 10 g/t) bioclastic limestone ore consists of quartz, dolomite, pyrite, illite, and trace Fe-dolomite, and these minerals are disseminated in ore (Fig. 4C-D). From least altered rock to high-grade ore, quartz, dolomite, pyrite, and illite significantly increase, and calcite decreases. Gold is dominantly in the arsenian pyrite as invisible Au, and the Au-bearing pyrite commonly rims a pre-ore-stage pyrite core or forms individual crystals (Fig. 4C-D; Xie et al., 2018a; 2018b).

Irregular masses of dolomite occur in medium- and high-grade samples and generally intergrows with quartz, Au-bearing pyrite, and illite (Fig. 4C-D). Locally, fine-grained Au-bearing pyrite is disseminated in dolomite. Dolomite encompassing anhedral residual Fe-dolomite is commonly observed in mineralized samples (Fig. 4D; Figs. 20H-I, Xie et al., 2018a). Scanning electron microscopy EDS analyses show that the Fe in dolomite is typically below the detection limit (~1 wt%).

4.2. Major and trace elements

Whole rock major and trace element compositions are listed in Table 1 and Appendix Table S1, and partial data are plotted in Fig. 5. The samples contain 0.84–14.87% MgO, 9.40–48.23% CaO, 3.11–54.66% SiO_2, and 0.13–3.40% S (Table 1). Carlin-suite elements (Au, As, Hg, Sb, Tl, and Cu) variably increase in the samples (Table 1). For moderate and intensive altered samples (Au > 0.1 g/t), their MgO contents are commonly higher than the regular limestone (MgO < 1–2%) (Table 1). Additionally, MgO shows a positive correlation trend with S, SiO_2, and Carlin-suite elements (Au, As, Hg, Sb, Tl, and Cu), and a negative correlation with CaO when the MgO concentration is less than ~ 6–8% (Fig. 5). However, MgO exhibits a reverse correlation trend with these elements when the MgO concentration is greater than ~ 6–8% (Fig. 5).

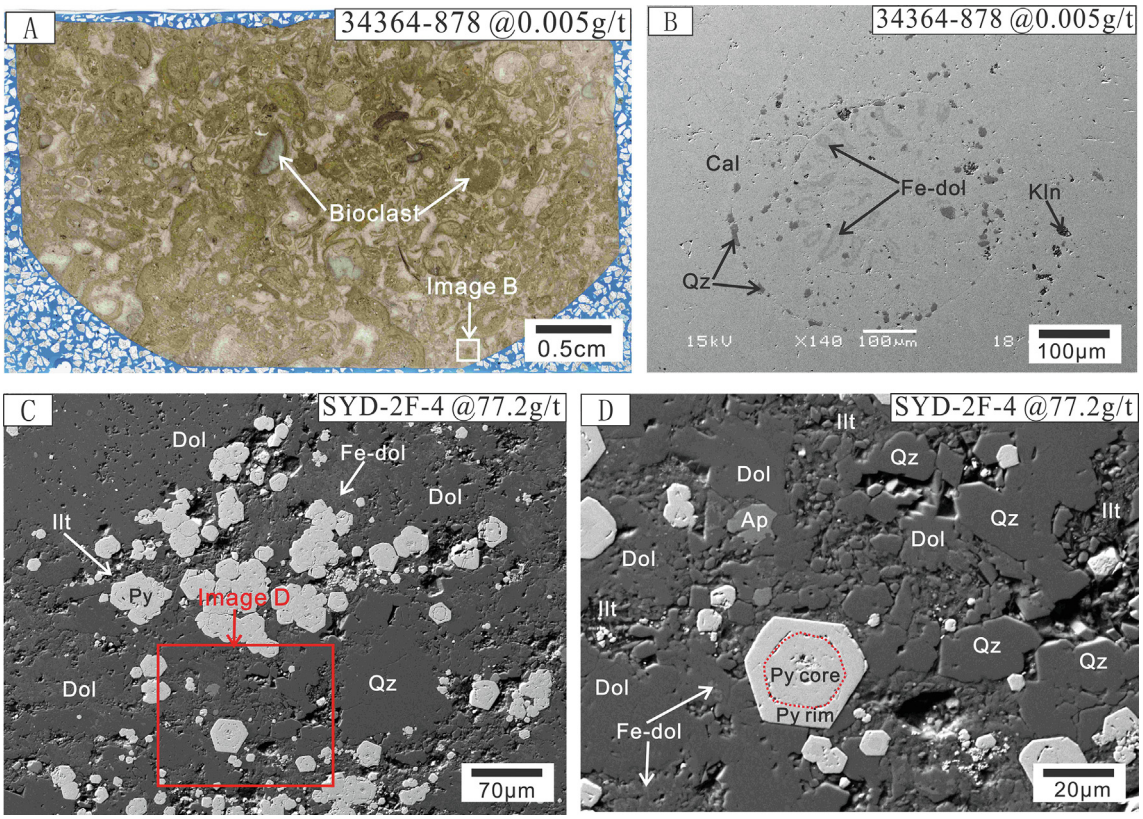

Fig. 4. Images of least altered bioclastic limestone (A, B) and high-grade bioclastic limestone ore (C, D) from the Shuiyindong deposit. The label in the upper right corner indicates the sample number and Au grade. A-B. Low grade bioclastic limestone is dominated by abundant bioclasts and calcite, minor Fe dolomite, and trace quartz and kaolinite (A: polished section scan image; B: backscattered electron images [BSE] image) (Xie et al., 2018a). C-D. High-grade limestone ore exhibits abundant pyrite, dolomite, quartz, minor illite, and trace Fe dolomite and apatite (BSE image). Gold mainly occurs in the pyrite rim as invisible Au. Abbreviations: Ap = apatite, Cal = calcite, Dol = dolomite, Fe-dol = Fe-dolomite, Kln = kaolinite, Py = pyrite, Qz = quartz.

Comparison of a strongly mineralized ore to the corresponding host rock using isocon diagram may reflect elemental fluxes and mass transfer associated with mineralization and alteration (Grant, 1986). Because the samples in this study were collected from three different layers (Fig. 3B), three isocon diagrams were generated (Fig. 6B-D). For each isocon diagram, two samples for comparison were from the same layer, with the high-grade sample from the anticline core and the barren sample from the limb and far from the high-grade sample. Aluminum, Ti, Th, Nb, and Zr were identified as immobile elements because of their high positive correlations among each other (Fig. 6A) and were utilized to generate immobility isocon. Elements plotting along the immobility isocon represent no net change or immobility. Elements plotting above the immobility isocon are added into the rock during mineralization and alteration. Elements plotting below the immobility isocon are removed from the rock.

The isocon diagrams (Fig. 6B-D) show Carlin-suite elements (except Cu) and S have been significantly and consistently added to the original rock in all three layers. Mg is added in the Longtan layer and remains nearly constant in the Changxing and Yelang layers. Silicon is added in the Changxing and Yelang layers and removed in the Longtan layer. Sodium is consistently removed. The net mass changes for all three layers, calculated by the equation: △mass (%) = [(1/m)-1]*100, are negligible (Fig. 6B-D).

4.3. Mg-C-O isotopes

The Mg-C-O isotopic compositions for bulk carbonates were analyzed because carbonate minerals are disseminated in samples, and it is difficult to separate the different types of carbonates. Results are given in Table 1. The δ^{26}Mg values have a wide range from −3.49‰ to −0.07‰, with a median value of −1.01‰. The δ^{18}O values range from 21.7‰ to 27.6‰, with a median value of 23.2‰. The δ^{13}C values vary from −14.6‰ to 1.2‰, with a median value of −0.7‰.

Fig. 3 shows the spatial distribution of δ^{26}Mg values in the cross section. For a particular layer, samples from the anticline core are commonly enriched in heavier Mg isotope than samples from the limbs (Fig. 3A). This is consistent with high-grade samples being mainly hosted in the anticline core. Exceptionally, two samples (23940–9 and 23940–43) collected from the limb have relatively heavier Mg isotopic compositions, with the δ^{26}Mg value of −1.33‰ and −0.07‰, respectively (Fig. 3).

Table 1
Mg-C-O isotopic compositions of bulk carbonate and part major and trace element compositions of whole rock from the Shuiyindong deposit.

Sample no.	Sampling location	Lithology	$\delta^{25}Mg$		$\delta^{26}Mg$		$\delta^{13}C$	$\delta^{18}O$	SiO_2	MgO	CaO	S	Au	Hg	As	Sb	Tl	Cu
			(‰)	2SD	(‰)	2SD	(‰)	(‰)	(%)	(%)	(%)	(%)	(10^{-6})	(10^{-6})	(10^{-6})	(10^{-6})	(10^{-6})	(10^{-6})
23909–17	First unit of YL Fm.	Muddy limestone	−0.38	0.01	−0.74	0.02	0.7	23.8	10.88	1.34	44.51	0.36	0.0243	0.1453	9.8	0.19	0.08	20.3
23905–12	First unit of YL Fm.	Muddy limestone	−0.44	0.07	−0.77	0.06	−2.2	22.4	32.11	2.00	26.30	2.58	13.8400	26.7853	3752.0	110.00	8.77	48.6
23940–6	First unit of YL Fm.	Muddy limestone	−0.46	0.01	−0.85	0.03	−0.5	23.1	16.41	1.71	39.76	0.22	0.0033	0.2962	18.6	0.41	0.06	40.7
23924–9	First unit of YL Fm.	Muddy limestone	−0.38	0.06	−0.71	0.05	1.2	23.3	23.61	2.82	29.39	0.22	0.0039	0.2637	3.0	0.13	0.04	61.9
23916–6	First unit of YL Fm.	Muddy limestone	−0.20	0.02	−0.42	0.02	−5.3	22.7	35.70	4.02	12.08	0.67	0.0044	0.3557	19.7	0.56	0.22	103.0
23908–5	First unit of YL Fm.	Muddy limestone	−0.57	0.02	−1.07	0.06	0.6	22.8	24.08	3.23	26.97	0.33	0.0112	0.1093	3.4	0.12	0.07	80.1
23902–20	First unit of YL Fm.	Muddy limestone	−0.21	0.03	−0.44	0.05	−0.1	23.9	21.04	2.16	32.52	0.41	1.0040	3.6820	30.1	0.19	0.36	50.1
23919–18	First unit of YL Fm.	Muddy limestone	−0.32	0.02	−0.62	0.05	0.0	23.8	21.58	2.46	31.85	0.22	0.0014	0.1981	15.1	0.22	0.09	57.4
23940–09	CX Fm.	Bioclast limestone	−0.72	0.13	−1.33	0.10	0.9	22.7	16.51	1.85	39.56	0.15	0.0015	0.1359	3.4	0.29	0.07	22.5
23924–16	CX Fm.	Bioclast limestone	−1.68	0.08	−2.98	0.10	1.1	22.3	19.14	0.84	43.29	0.16	0.0012	0.0793	2.9	0.28	0.01	3.7
23916–14	CX Fm.	Bioclast limestone	−0.35	0.06	−0.60	0.06	1.1	22.6	8.54	1.19	48.23	0.13	0.0009	0.0850	2.5	0.16	0.02	7.6
23908–12	CX Fm.	Bioclast limestone	−0.35	0.09	−0.60	0.09	−0.6	22.3	54.66	1.79	14.64	0.43	0.0021	0.3450	14.9	0.45	0.24	28.3
23902–32	CX Fm.	Bioclast limestone	−0.60	0.04	−1.14	0.06	−0.7	21.7	42.15	1.55	26.72	0.71	2.0490	6.8208	623.0	8.09	0.68	21.1
23905–32	CX Fm.	Bioclast limestone	−1.09	0.07	−1.96	0.08	0.3	22.7	15.41	1.37	43.29	0.61	0.0446	2.1953	226.0	2.73	0.16	13.0
23909–32	CX Fm.	Bioclast limestone	−1.99	0.10	−3.49	0.06	0.6	23.3	3.11	0.96	52.21	0.25	0.0089	0.3998	4.8	0.24	0.04	3.9
23919–24	CX Fm.	Bioclast limestone	−1.71	0.09	−3.00	0.14	0.7	23.2	9.60	1.36	46.40	0.28	0.0025	0.1608	1.9	0.19	0.06	8.5
23902–70	Third unit of LT Fm.	Limestone	−0.51	0.04	−0.98	0.03	−3.5	23.2	42.43	4.30	9.40	2.99	2.5050	7.6416	2403.0	18.70	1.54	59.7
23908–30	Third unit of LT Fm.	Bioclast limestone	−0.34	0.04	−0.68	0.07	−2.7	23.8	39.24	5.66	13.96	3.40	0.0020	22.1350	1597.0	20.10	1.50	57.0
23940–43	Second unit of LT Fm.	Limestone	−0.04	0.05	−0.07	0.08	−5.4	22.7	42.05	4.71	17.74	0.17	0.0121	0.0908	4.7	0.10	0.10	22.0
23924–45	Second unit of LT Fm.	Limestone	−0.97	0.06	−1.84	0.06	−3.0	21.7	12.66	3.03	43.85	0.43	0.0450	0.4933	74.5	0.99	0.15	4.2
23916–42	Second unit of LT Fm.	Limestone	−0.38	0.01	−0.72	0.07	−3.3	23.8	32.68	8.48	18.02	3.05	5.6700	5.7572	1865.0	16.50	1.93	44.9
23908–54	Second unit of LT Fm.	Limestone	−0.63	0.10	−1.17	0.09	−3.1	23.6	26.55	8.73	26.10	2.84	4.2450	11.6080	1851.0	59.90	3.07	22.5
23902–97	Second unit of LT Fm.	Limestone	−0.66	0.07	−1.25	0.04	−3.6	24.5	33.11	10.75	19.69	1.90	1.2880	12.1969	727.0	22.60	1.47	18.4
23905–58	Second unit of LT Fm.	Bioclast limestone	−0.59	0.06	−1.04	0.12	−4.6	25.0	20.40	12.18	22.16	2.84	23.5800	0.0024	1556.0	906.00	1.45	23.5
23909–65	Second unit of LT Fm.	Limestone	−1.12	0.05	−2.13	0.06	−14.5	24.0	6.63	14.87	33.38	0.35	0.0047	0.1809	22.6	2.59	0.09	6.1
23919–43	Second unit of LT Fm.	Limestone	−1.23	0.02	−2.32	0.04	−12.3	27.6	10.71	12.91	29.70	0.16	0.0016	0.2936	14.1	0.35	0.01	3.2

Note the sample number consists of drill hole number and sampling depth (meter). All major and trace element concentrations are provided in Appendix Table S1.
Tan et al. (2017) also reported the C and O isotopes data of the second unit of Longtan Formation. Our analysis results are consistent with their data.
Abbreviations: CX Fm. = Changxing Formation, LT Fm. = Longtan Formation, YL Fm. = Yelang Formation.

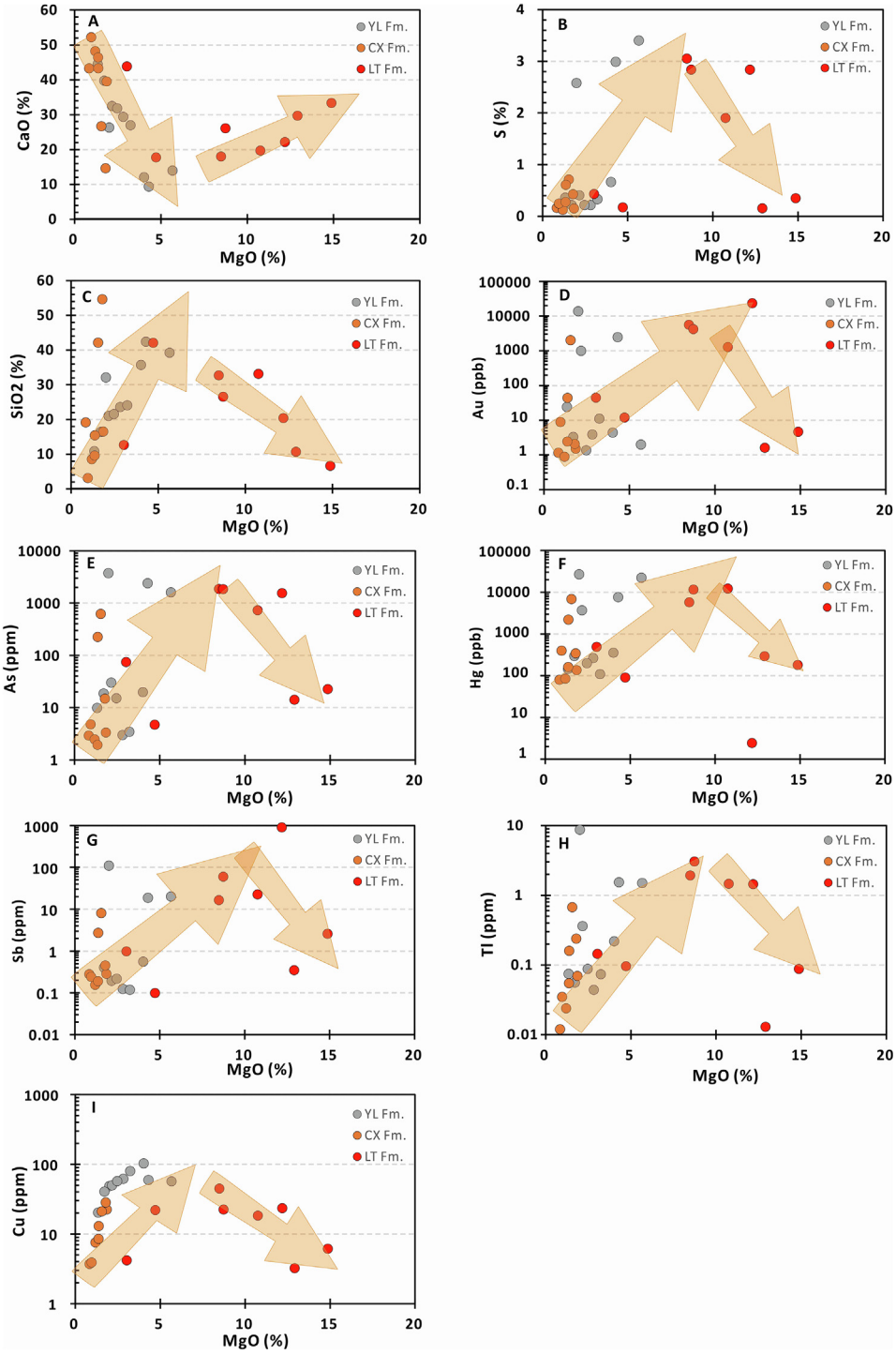

Fig. 5. Plots of MgO versus CaO, S, SiO_2, and Carlin-suite elements including Au, As, Hg, Sb, Tl, and Cu. When the MgO concentration is less than ~ 6–8%, MgO shows a negative correlation trend with CaO (A) and a positive correlation with S (B), SiO_2(C), and Carlin-suite elements (Au, As, Hg, Sb, Tl, and Cu) (D-I); When the MgO content is greater than ~ 6–8%, MgO exhibits a reverse correlation trend with these elements, and the samples are from the Longtan Formation. This may indicate that intensive Au (and other Carlin-suite elements) mineralization commonly accompanies moderately dolomitization (MgO: ~6–8%). Too intensive or weak dolomitization would lower the Au grade. Abbreviations: YL Fm. = Yelang Formation, CX Fm. = Changxing Formation, LT Fm. = Longtan Formation.

Fig. 7 exhibits the δ^{26}Mg values that have a negative correlation trend with CaO, a positive correlation trend with MgO, S, SiO_2, and Carlin-suite elements (Au, As, Hg, Sb, Tl, and Cu). Samples with low CaO, high MgO, S, SiO_2, and Carlin-suite elements are commonly enriched with δ^{26}Mg greater than ~ -1.5‰ (Fig. 7), and these sam-

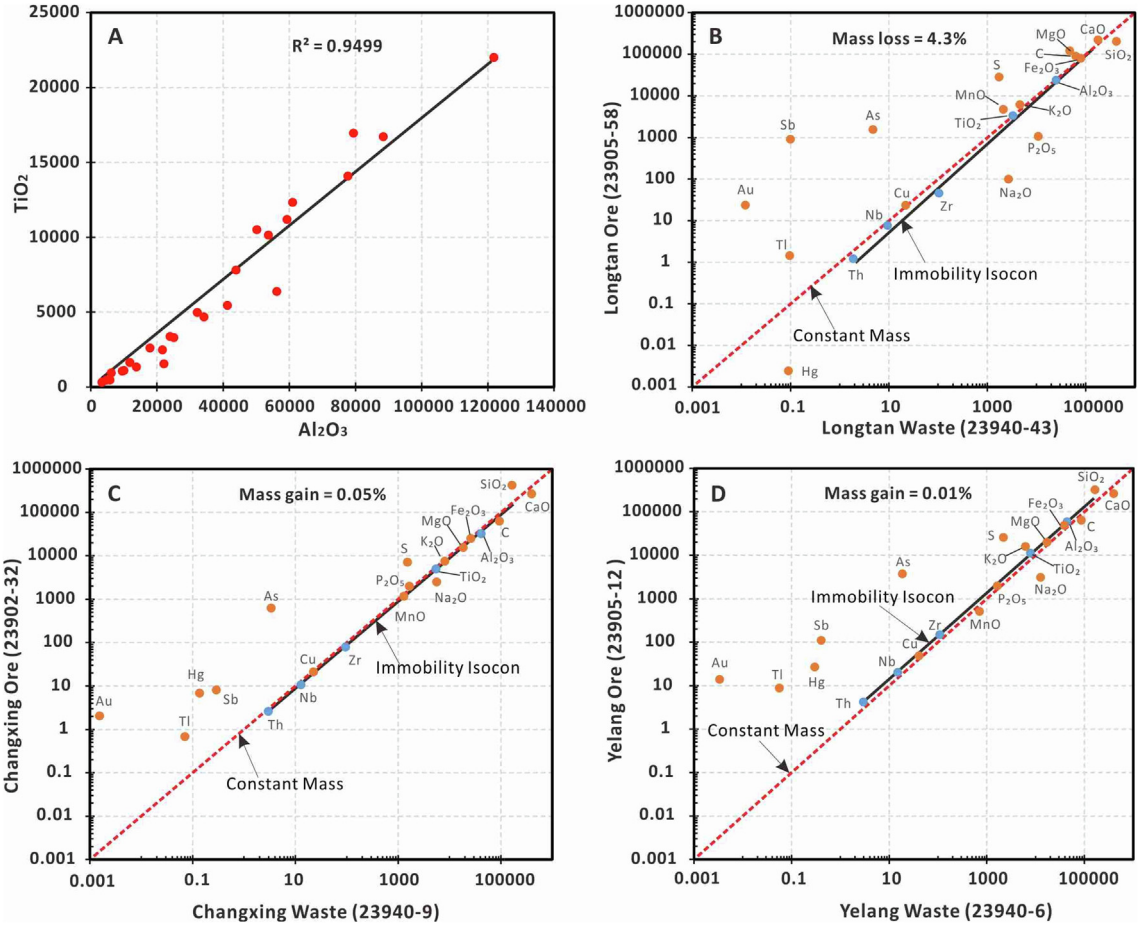

Fig. 6. Plot of the concentrations of TiO_2 vs. Al_2O_3 (A) and isocon diagrams showing major and Carlin-suite elements fluxes and mass transfer associated with Au mineralization at the Shuiyindong deposit (B-D). All values are in ppm and included in Appendix Table S1. The high positive correlation ($R^2 = 9499$) between TiO_2 and Al_2O_3 reflects that these species are immobile components at the deposit (A). By similar methods, Th, Nb, and Zr were also identified as immobile elements. The immobility isocon is the line of best fit through the concentrations of TiO_2, Al_2O_3, Zr, Nb, and Th. The net mass change is calculated by the equation: $\triangle$mass (%) = [(1/m)-1]*100, where m is the slope of the immobility isocon (Hofstra, 1994). Gold, As, Sb, Hg, Tl, and S are consistently added (B-D). MgO is added in the Longtan layer (B) and remains nearly constant in the Changxing and Yelang layers (C-D). SiO_2 is added in the Changxing and Yelang layers (C-D) and removed in the Longtan layer (B).

ples are more extensively altered compared with samples with δ^{26}Mg less than ~ -1.5‰. Note that some samples with δ^{26}Mg values greater than ~ -1.5‰, however, do not show enrichment of MgO, S, SiO_2, and Carlin-suite elements, nor loss of CaO. These samples are mainly from the Yelang and Changxing Formations (Fig. 7).

Fig. 8 integrates the Carlin-suite elements, δ^{26}Mg, δ^{18}O, and δ^{13}C values of all samples according to the stratigraphy. Overall, the Carlin-suite elements exhibit a highly consistent variation trend (Fig. 8). As Carlin-suite elements' concentrations increase, the δ^{26}Mg values increase, δ^{13}C values slightly decrease, and δ^{18}O values display an insignificant variation (Fig. 8). Two samples from the Longtan Formation (23909-65, 23919-43) have a relatively low δ^{13}C (Fig. 8), and this could be a result of an increase of organic matter as these two samples are darker than other samples.

5. INTERPRETATION AND DISCUSSION

5.1. Formation of dolomite and its relationship to Au mineralization

Mg-bearing dolomite is abundant in ore but absent in bioclastic limestone host rock in the Shuiyindong deposit (Fig. 4). Thus, Mg-bearing dolomite was variably added to ore during Au mineralization. The Mg was mainly fixed in the ore-stage dolomite because of the absence of other Mg-rich minerals in ore. Additionally, formation of ore-stage dolomite (dolomitization) is a widespread alteration process in clastic rocks (e.g., Jinfeng and Yata, Su et al., 2009; Xie et al., 2018a) and basaltic rocks-hosted Carlin-type Au deposits (e.g., Jiadi and Damaidi, Li et al., 2021) in the Youjiang Basin. Dolomite-stable alteration in Guizhou Carlin-type Au deposits reflects a near-neutral acidity

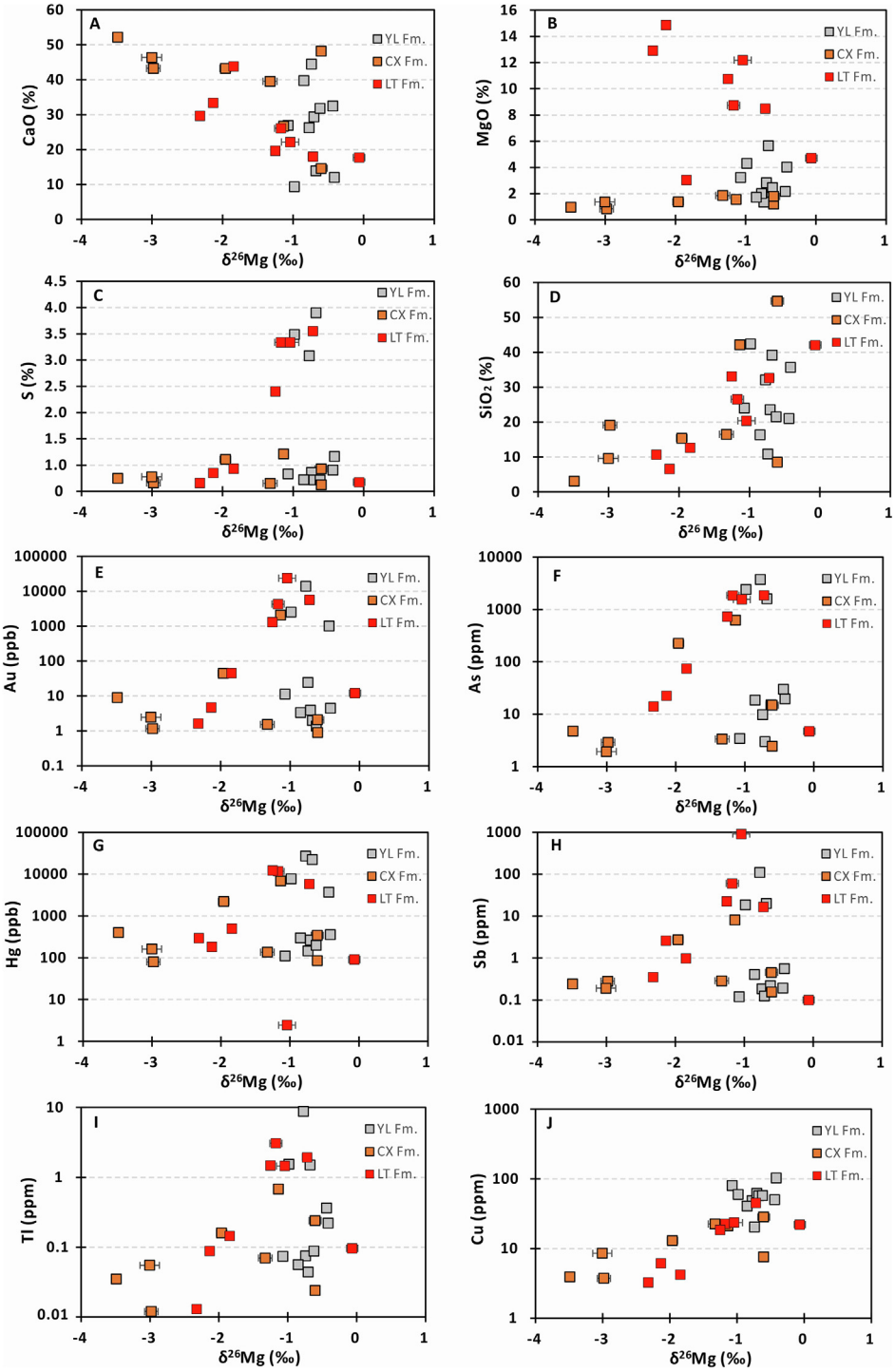

Fig. 7. Plots of δ^{26}Mg versus CaO, MgO, S, SiO_2, and Carlin-suite elements including Au, As, Hg, Sb, Tl, and Cu. The δ^{26}Mg values have a negative correlation trend with CaO (A), a positive correlation trend with MgO (B), S (C), SiO_2 (D), and Carlin-suite elements (Au, As, Hg, Sb, Tl, and Cu) (E-J). Samples with low CaO, high MgO, S, SiO_2, and Carlin-suite elements are commonly enriched with δ^{26}Mg value greater than ~ -1.5‰, and these samples are more extensively altered compared with samples with δ^{26}Mg less than ~ -1.5‰. Abbreviations: YL Fm. = Yelang Formation, CX Fm. = Changxing Formation, LT Fm. = Longtan Formation.

of ore fluids, which removed calcite but could not remove dolomite (Xie et al., 2017; 2018a).

We propose two possible origins for the ore-stage dolomite in the Shuiyindong deposit: (a) ore fluids sulfidized Fe in Fe-dolomite to form Au-bearing pyrite and dolomite (Xie et al., 2017; 2018a); and (b) Mg in ore fluids combined with calcite to form dolomite. It is difficult to identify the active process based on petrographic observation.

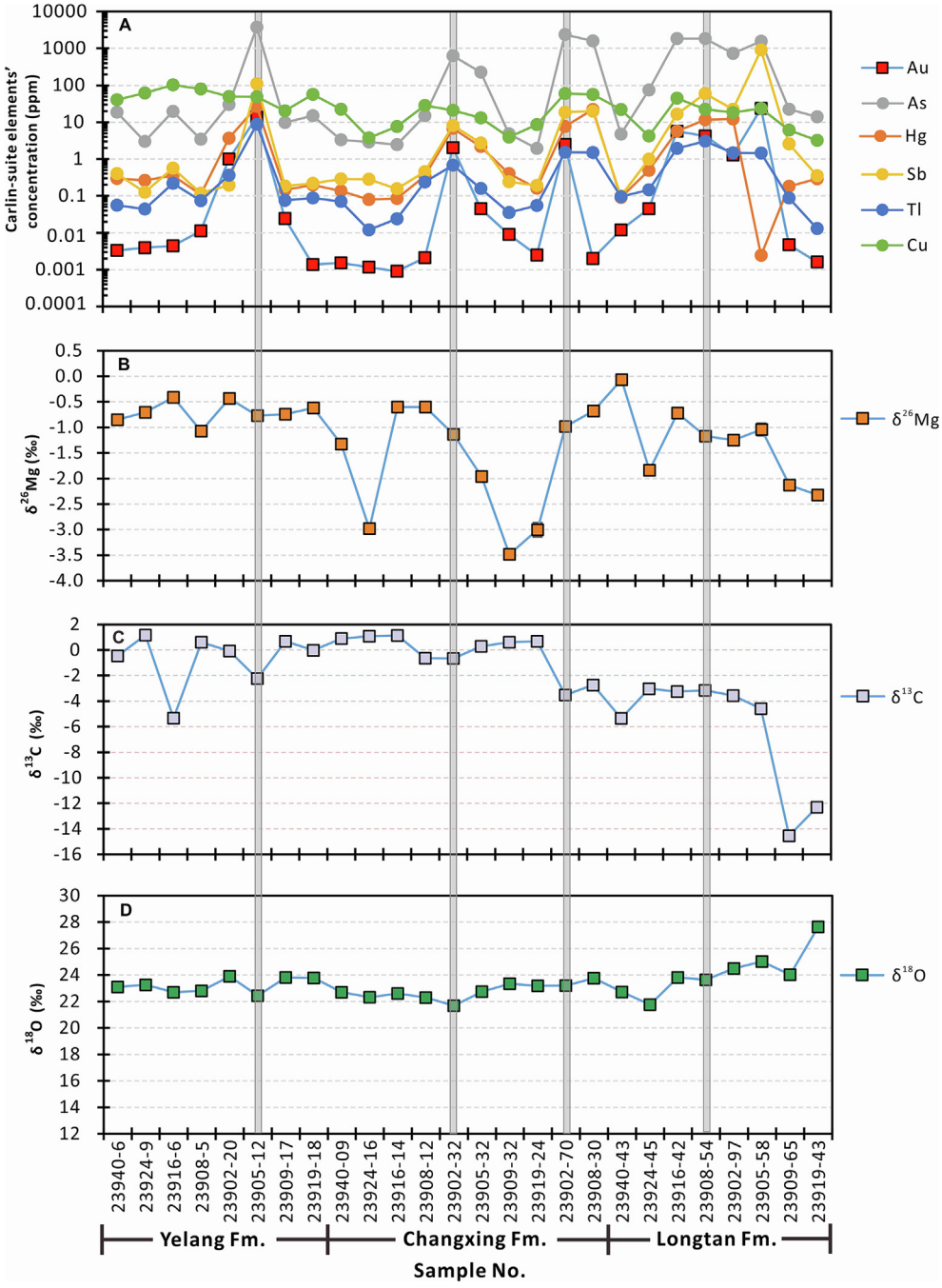

Fig. 8. Variations of Carlin-suite elements (Au, As, Hg, Sb, Tl, and Cu) (A), δ^{26}Mg (B), δ^{13}C (C), and δ^{18}O (D) of the samples collected from different formations. Carlin-suite elements show a highly coordinated variation (A). As Carlin-suit elements' concentrations increase, the δ^{26}Mg values increase (B), and δ^{13}C values slightly decrease (C), however, δ^{18}O values don't show a significant variation (D). Samples 23909–65 and 23919–43 have a relatively low δ^{13}C (C), and these could be a result of an increase of organic matter.

However, a small amount of dolomite should form by the addition of Mg to calcite because (1) MgO shows a positive correlation trend with Carlin-suite elements which reflects that Mg was variably added during mineralization (Fig. 5); and (2) individual fluid inclusion study shows that the Mg concentration in ore fluids decreased from up to 200 ppm to below the detection limit of LA-ICP-MS from the main-ore to late-ore stages (Su et al., 2009), and the reduced Mg was likely fixed into the dolomite. Note that the isocon diagram suggests that Mg was added or immobile instead of uniformly added during mineralization (Fig. 6B-D). This is because the Mg concentration in protolith varies greatly (e.g., samples with Au concentration<10 ppb have a wide range of MgO from 0.84% to 14.87%), and the variable and relatively limited addition of Mg can't significantly change the Mg concentration of

protolith. Hence, although the isocon diagram suggests Mg is immobile, it is still possible that a small amount of Mg could have been added into the rock during mineralization.

5.2. Origin of heavy Mg isotopic compositions in carbonate

Comparison of Mg isotope data from this study with the major reservoirs shows the Shuiyindong samples contain isotopically heavier Mg isotopes compared with the normal carbonate and drifts towards heavy Mg reservoirs (Fig. 9). Petrographic observation and chemical analysis suggest that the Mg is dominantly hosted in the dolomite, which is a major Mg sink during carbonate deposition. Thus, the $\delta^{26}Mg$ of dolomite basically represents the Mg isotopic composition of carbonate fractions. Li et al. (2015) performed hydrothermal experiments to calibrate the Mg isotope fractionation between hydrothermal dolomite and aqueous solution, and results defined a temperature-fractionation function for Mg in dolomite: $\Delta^{26}Mg_{dolo\text{-}aq} = -0.1554(\pm 0.0096)* 10^6/T^2$, where T is in Kelvin. Using this function, we calculated the Mg isotopic composition of ore fluids at a temperature of ~ 280 °C, and results suggest that: $\delta^{26}Mg_{aq} = \delta^{26}Mg_{dolo} + 0.51‰$. Collectively, the ore fluids should have had $\delta^{26}Mg$ values basically equal to $\delta^{26}Mg_{carb}$ plus 0.51‰, drifting towards the heavy Mg reservoirs.

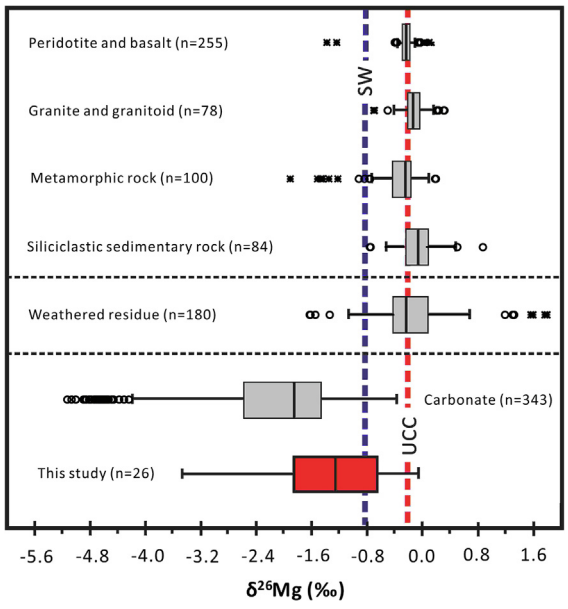

Fig. 9. Comparison of Mg isotope data of this study with the major reservoirs showing the $\delta^{26}Mg$ values for carbonate fractions in bulk samples from the Shuiyindong deposit are greater than that of the normal carbonate worldwide and drift towards the reservoirs enriched with heavy Mg isotope (modified from Huang et al., 2015). The box encompasses the 25 and 75 percentiles, the vertical line inside the box indicates the median value, the whiskers represent the 2.5 and 97.5 percentiles, and the gray dots are outliers. The blue and red vertical dashed lines indicate the average $\delta^{26}Mg$ of seawater (SW, −0.83‰) (n = 47) and upper continental crust (UCC, −0.22‰) (n = 32), respectively.

Previous studies suggested two distinguishing ore fluids, including shallow fluids (basin fluid or meteoric water) (Liu et al., 2001; Wang et al., 2002; Hu et al., 2017) or deep fluids (metamorphic or magmatic fluid) (Su et al., 2009; 2018; Xie et al., 2018b; Jin et al., 2020; Zhu et al., 2020), possibly have formed the Guizhou deposits. If ore fluids are basin fluid or evolved from the meteoric water, the ore-forming elements would have been leached from the sedimentary rocks, and Mg in the ore fluids should be most likely from the carbonates in the basin. Because light Mg preferentially releases and enters the fluid during fluid-rock reaction (Galy et al., 2002; Tipper et al., 2006, 2012; Teng et al., 2010; Huang et al., 2012; Li et al., 2014; Teng, 2017), ore fluids should be enriched in lighter Mg and ultimately form ore-stage dolomite with lighter Mg isotope compared to the normal carbonate. This is inconsistent with our observation because our results indicate the heavier Mg was added during Au mineralization (Figs. 7-9). Thus, the Mg isotope data oppose a sedimentary source of ore-forming elements.

Our results support a model with ore fluids released from magmatism or metamorphism because the Mg isotope data of ore fluids drifting toward the magmatic and metamorphic rocks ends. Because the sedimentary rocks that compose the Youjiang Basin did not undergo metamorphism, a potential magmatic Mg source is more likely. Known igneous rocks in the basin are scarce; however, some quartz porphyry dikes and alkaline ultramafic dikes do occur within or 10–30 km from the Au deposits (Fig. 1; Xie et al., 2018b). Dating on inherited zircons from quartz porphyry dikes in Liaotun, Bama, and Xiabaha districts shows age clusters of 130–140 Ma and ca. 242 Ma (Zhu et al., 2016). These ages were interpretated ages of deep hidden intrusions in these areas. Additionally, geophysical investigation (gravity and magnetic) in the southwest Guizhou Province indicated the presence of several hidden batholiths ~ 5 km below the surface, and most Carlin-type Au deposits in the district are located within the region indicated by the inferred batholith (Liu, et al., 2017). Collectively, we suggest the thick (6–12 km) Devonian-Triassic sedimentary sequence in the Youjiang Basin, and weak extension following sedimentation, prevented igneous activity from reaching the surface (Xie et al., 2018b). However, buoyant ore fluids released from the intrusions could have ascended along the basement-penetrating faults and precipitated Au at shallow levels.

The deep magmatic signals were recorded by the isotopes of the exsolved ore fluids. For example, the ore fluids released from deep intrusions inherited the Mg isotopic composition of magmatic rocks because fluid exsolution has a limited Mg isotopic fractionation (Teng, 2017). While ore fluids ascended and cooled, the Mg isotopes did not fractionate significantly because there is no evidence indicating Mg-rich minerals precipitated during this process. Eventually during Au mineralization, Mg from ore fluids was added as dolomite precipitated, and the original magmatic Mg signature was recorded by the dolomite. In addition to Mg isotopes, the Hg (Yin et al., 2019), S (Xie et al., 2018b; Li et al., 2020a), and noble gas (He-Ne-Ar) (Jin et al., 2020) isotopes all reflect magmatic signals of ore fluids.

Considering the isocon diagrams suggesting a variable and relatively limited addition of Mg during Au mineralization (Fig. 6B-D), isotopic equilibrium exchange is also a potential mechanism attributed to heavy Mg isotopic compositions in carbonates. In theory, as long as the Mg-rich ore fluids have δ^{26}Mg values distinguished from the carbonates, Mg isotope exchange reaction would occur when ore fluids reacted with carbonates. As fluid-rock reaction proceeds, the carbonates will become partially or even totally fluid-buffered with respect to Mg isotopes. The samples in this study contain Mg isotopic compositions heavier than the typical carbonates (Fig. 9), reflecting ore fluids were enriched in heavy Mg. Because it is difficult to calculate the content of the added Mg and almost impossible to distinguish the added Mg from the exchanged Mg, the dominated mechanism (heavy Mg addition from ore fluids or isotopic exchange reaction with heavy Mg-rich ore fluids) attributed to heavy Mg in carbonates remains indistinguishable. Nevertheless, ore fluids were enriched in heavy Mg, and they were most likely released from the deep intrusions.

5.3. Genesis of the Guizhou Carlin-type Au deposits

Post-collisional extension of the Indochina orogen and far-field effects related to subduction of the Paleo-Pacific plate triggered formation of deep magmas. These igneous activities did not reach the surface because of the thick sedimentary sequences in the Youjiang Basin. Buoyant ore fluids released from deep magma ascended along basement-penetrating faults and converged at culminations (e.g., anticlines and domes). The near-neutral ore fluids reacted with Fe-rich carbonate rocks, and Fe in Fe-dolomite was sulfidized to form Au-bearing pyrite and dolomite (Xie et al., 2017; 2018a; Su et al., 2018). Additionally, a small amount of calcite combined with Mg from ore fluids to form dolomite, though most calcite was dissolved and replaced by jasperoid quartz. Ore fluids also reacted with silicate minerals in the host rocks (e.g., muscovite and K-feldspar) forming minor illite associated with ore pyrite (Xie et al., 2018a; Su et al., 2018).

At the Shuiyindong deposit, ore fluids ascended to the unconformity (SBT), and then migrated horizontally along the unconformity, and converged at the Huijiabao anticline (Tan et al., 2015; Liu et al., 2020). There, ore fluids ascended into the overlying strata along the anticlinal axis and reacted with the bioclastic limestone and precipitated Au from the anticlinal axis toward the limbs. Thus, the axis commonly exhibits stronger Au mineralization than the limbs, and more Mg from ore fluids was added to the axis and/or exchanged with Mg from the axis host rocks. Eventually, the axial area exhibits δ^{26}Mg values indicating magmatism, whereas the limbs display δ^{26}Mg values closer to carbonate values (Fig. 3). Collectively, the direction of increasing of δ^{26}Mg values may indicate a mineralization center.

Unlike the Nevada Carlin-type Au deposits, where ore fluids have altered the original O isotopes because of intensive decarbonatization and isotopic exchange reaction, resulting in a significant O isotope altered halo (Barker et al., 2013; Vaughan et al., 2016), the Guizhou Carlin-type Au deposits have limited addition and exchange of O and C isotopes from ore fluids during Au mineralization, and almost all O and C in ore was inherited from the sedimentary strata. Thus, there is no significant magmatic signals from C and O isotopic compositions and a limited correlation between the C-O isotopes and Carlin-suite elements (Fig. 8).

5.4. Implications for Mg isotope tracers in ore deposits

The Mg isotopes have a larger variation in different reservoirs, and the fractionation behavior during major geological processes is relatively well constrained. A few studies used the Mg isotopes to constrain the genesis of ore deposits, with focusing on magmatic ore deposits. For example, Tang et al. (2018) analyzed the Mg isotopic compositions of the intrusion and country rocks from the giant Jinchuan Ni-Cu-(PGE) sulfide deposit and found that the intrusion has δ^{26}Mg values slightly lighter than the mantle-derived magma. Combined with Sr-Nd isotopes data, they concluded that the Jinchuan intrusion underwent bulk contamination by lower continental crust and marbles, which led to the formation of the ore deposit. Another example is that Li et al. (2020b) compared the Mg isotopic compositions of the altered and unaltered rocks from the Dexing porphyry Cu deposit and found that the altered rocks typically have δ^{26}Mg values heavier than the unaltered rocks. Combined with δ^{26}Mg -δ^{41}K binary diagram, they suggested that three isotopically distinct ore fluid involved in the formation of the deposit. Our study further demonstrates that Mg isotopes are a novel proxy to infer ore fluids source and provide significant constraints on the genesis of Carlin-type Au deposits. Thus, the Mg isotopes are a potential excellent tracer to constrain sources and the evolution of the Mg-rich ore fluids.

Many hydrothermal deposits exhibit precipitation of ore-stage Mg-rich minerals. For example, orogenic Au deposits typically have ore-related sericite and carbonate; MVT-type Pb-Zn deposits commonly show formation of ore-stage dolomite. However, the relationships of these deposits to the deep geological events (e.g., deep magmatic activities) have been controversial. Study of Mg isotopes on the ore-stage Mg-rich minerals can provide new constraints on the ore fluid source and evolution and genesis of the deposits.

6. CONCLUSIONS

Guizhou Carlin-type Au deposits exhibit the formation of abundant ore-stage dolomite during Au mineralization. Petrographic observations and chemical analyses indicate that some ore-stage dolomite formed by the combination of host rock calcite with Mg from ore fluids during the Au mineralization process, although most ore-stage dolomite formed during sulfidation of Fe in the Fe-dolomite to form Au-bearing pyrite and Mg-bearing dolomite.

We first investigated the Mg isotopic compositions of the giant Shuiyindong Carlin-type Au deposit. The δ^{26}Mg values of bulk carbonates in samples range from −3.49‰

to −0.07‰, with a median value of −1.01‰. These values are significantly greater than those of the normal carbonate and drift toward the heavy Mg reservoirs. Heavy Mg isotope values in the Shuiyindong deposit are resulted by the addition of heavy Mg from ore fluids and/or by isotopic exchange reaction with heavy Mg-rich ore fluids.

We propose a model in which ore fluids enriched in heavy Mg were released from a deep intrusion, and ascended along basement-penetrating faults and converged at culminations (e.g., anticlines and domes). Where ore fluids encountered Fe-bearing and carbonate-rich host rocks at appropriate conditions, ore fluids reacted with the host rocks, forming Au-bearing pyrite and, ultimately, the Guizhou Carlin-type Au deposits. During Au mineralization, Mg in ore fluids was added to ore, and/or was exchanged with Mg from host rocks, and to form ore-stage dolomite with heavy Mg isotopic compositions.

This study implies that Mg isotopes are a novel proxy to infer ore fluids source and evolution. Hydrothermal deposits commonly exhibit precipitation of ore-stage Mg-rich minerals. The Mg isotopes could be effectively applied to study the genesis of many hydrothermal deposits.

DECLARATION OF COMPETING INTEREST

The authors declare that they have no known competing financial interests or personal relationships that could have appeared to influence the work reported in this paper.

ACKNOWLEDGEMENTS

We appreciate Guizhou Zijin Mining Corporation for access to the Shuiyindong deposit for sampling. We would like to thank Zekun Meng from the Northwest University, Xi'an, China, for assistance with Mg isotopes analysis, and Shengwei Wu and Jing Gu from the Institute of Geochemistry, Chinese Academy of Sciences (IGCAS) for C-O isotopes analyses. Editor-in-chief Dr. Jeffrey Catalano, associated editor Dr. Adam Simon, and an anonymous reviewer are thanked for their constructive comments and suggestions which have significantly improved the manuscript. We are particularly grateful to Dr. Shaun Barker for his insightful comments, suggestions, and in-depth discussions, which have greatly improved the manuscript. This research was financially supported by grants from the National Natural Science Foundation of China (42073044; U1812402; 41703046), the Guizhou Provincial Science and Technology Projects (Qiankehejichu[2020]1Z034; Qiankehepingtairencai-CXTD[2021]007), the Geological Exploration Fund Project of Guizhou Province (520000214TLCOG7DGTNRG), the West Light Foundation of the Chinese Academy of Sciences (xbzg-zdsys-202108), and the Youth Innovation Promotion Association, Chinese Academy of Sciences (2022402).

APPENDIX A. SUPPLEMENTARY MATERIAL

Supplementary material to this article can be found online at https://doi.org/10.1016/j.gca.2022.07.009.

REFERENCES

Bao Z. A., Huang K. J., Huang T. Z., Shen B., Zong C. L., Chen K. Y. and Yuan H. L. (2019) Precise magnesium isotope analyses of high-K and low-Mg rocks by MC-ICP-MS. *J. Anal. Atom. Spectrom.* **34**, 940–953.

Barker S. L. L., Dipple G. M., Hickey K. A., Lepore W. A. and Vaughan J. R. (2013) Applying stable isotopes to mineral exploration: Teaching an old dog new tricks. *Econ. Geol.* **108**, 1–9.

Chen M. H., Zhang Y., Meng Y. Y., Lu G. and Liu S. Q. (2014) The confirmation of the upper limit of metallogenetic epoch of Liaotun gold deposit in western Guangxi, China, and its implication on chronology of Carlin-type gold deposits in Yunnan-Guizhou-Guangxi "golden triangle" area. *Mineral Deposits* **33**, 1–13, in Chinese with English abstract.

Chen M. H., Bagas L., Liao X., Zhang Z. Q. and Li Q. L. (2019) Hydrothermal apatite SIMS Th-Pb dating: Constraints on the timing of low-temperature hydrothermal Au deposits in Nibao, SW China. *Lithos* **324–325**, 418–428.

Cline J. S., Hofstra A. H., Muntean J. L., Tosdal R. M. and Hickey K. A. (2005) Carlin-type gold deposits in Nevada: Critical geologic characteristics and viable models. *Econ. Geol.* **100th Anniv. Vol**, 451–484.

Du D. H., Li W. Q., Wang X. L., Shu X. J., Yang T. and Sun T. (2019) Fe isotopic fractionation during the magmatic-hydrothermal stage of granitic magmatism. *Lithos* **350–351**, 1–13.

Galy A., Bar-Matthews M., Halicz L. and O'Nions R. K. (2002) Mg isotopic composition of carbonate: Insight from speleothem formation. *Earth Planet. Sci. Lett.* **201**, 105–115.

Gao W., Hu R. Z., Hofstra A. H., Li Q. L., Zhu J. J., Peng K. Q., Mu L., Huang Y., Ma J. W. and Zhao Q. (2021) U-Pb dating on hydrothermal rutile and monazite from the Badu gold deposit supports an early Cretaceous age for Carlin-type gold mineralization in the Youjiang Basin, Southwestern China. *Econ. Geol.* **116**, 1355–1385.

Geske A., Lokier S., Dietzel M., Richter D. K., Buhl D. and Immenhauser A. (2015) Magnesium isotope composition of sabkha porewater and related (Sub-)Recent stoichiometric dolomites, Abu Dhabi (UAE). *Chem. Geol.* **393–394**, 112–124.

Grant J. A. (1986) The isocon diagram-a simple solution to Gresens' equation for metasomatic alteration. *Econ. Geol.* **81**, 1976–1982.

Hofstra A. H. and Cline J. S. (2000) Characteristics and models for Carlin- type gold deposits. *Rev. Econ. Geol.* **13**, 163–220.

Hofstra, A.H., 1994. Geology and genesis of the Carlin-type gold deposits in the Jerritt Canyon district, Nevada. Ph.D. dissertation Boulder, Colorado, University of Colorado, 719.

Hu R. Z., Fu S. L., Huang Y., Zhou M. F., Fu S. H., Zhao C. H., Wang Y. J., Bi X. W. and Xiao J. F. (2017) The giant South China Mesozoic low-temperature metallogenic domain: Reviews and a new geodynamic mode. *J. Asian Earth Sci.* **137**, 9–34.

Huang K. J., Teng F. Z., Wei G. J., Ma J. L. and Bao Z. Y. (2012) Adsorption- and desorption-controlled magnesium isotope fractionation during extreme weathering of basalt in Hainan Island. *China. Earth Planet. Sci. Lett.* **359–360**, 73–83.

Huang K. J., Shen B., Lang X. G., Tang W. B., Peng Y., Ke S., Kaufman A. J., Ma H. R. and Li F. B. (2015) Magnesium isotopic compositions of the Mesoproterozoic dolostones: Implications for Mg isotopic systematics of marine carbonates. *Geochim. Cosmochim. Acta* **164**, 333–351.

Huang K. J., Teng F. Z., Shen B., Xiao S. H., Lang X. G., Ma H. R., Fu Y. and Peng Y. B. (2016) Episode of intense chemical weathering during the termination of the 635 Ma Marinoan glaciation. *Proc. Natl. Acad. Sci. USA* **113**, 14904–14909.

Huang K. J., Teng F. Z., Plank T., Staudigel H., Hu Y. and Bao Z. Y. (2018) Magnesium isotopic composition of altered oceanic crust and the global Mg cycle. *Geochim. Cosmochim. Acta* **238**, 357–373.

Jin X. Y., Hofstra A. H., Hunt A. G., Liu J. Z., Yang W. and Li J. W. (2020) Noble gases fingerprint the source and evolution of ore-forming fluids of Carlin-type gold deposits in the golden triangles, South China. *Econ. Geol.* **115**, 455–469.

Jin X. Y., Zhao J. X., Feng Y. X., Hofstra A. H., Deng X. D., Zhao X. F. and Li J. W. (2021) Calcite U-Pb dating unravels the age and hydrothermal history of the jiant Shuiyindong Carlin-type gold deposit in the golden triangle, South China. *Econ. Geol.* **116**, 1253–1265.

Kesler S. E., Riciputi L. C. and Ye Z. J. (2005) Evidence for a magmatic origin for Carlin-type gold deposits: isotopic composition of sulfur in the Betze-Post-Screamer deposit, Nevada, USA. *Miner. Deposita* **40**, 127–136.

Large S. J. E., Bakker E. Y. N., Weis P., Wälle M., Ressel M. and Heinrich C. A. (2016) Trace elements in fluid inclusions of sediment-hosted gold deposits indicate a magmatic-hydrothermal origin of the Carlin ore trend. *Geology* **44**, 1015–1018.

Li W. Q., Beard B. L. and Johnson C. M. (2011) Exchange and fractionation of Mg isotopes between epsomite and saturated $MgSO_4$ solution. *Geochim. Cosmochim. Acta* **75**, 1814–1828.

Li W. Q., Beard B. L., Li C. X. and Johnson C. M. (2014) Magnesium isotope fractionation between brucite [$Mg(OH)_2$] and Mg aqueous species: Implications for silicate weathering and biogeochemical processes. *Earth Planet. Sci. Lett.* **394**, 82–93.

Li W. Q., Beard B. L., Li C. X., Xu H. F. and Johnson C. M. (2015) Experimental calibration of Mg isotope fractionation between dolomite and aqueous solution and its geological implications. *Geochim. Cosmochim. Acta* **157**, 164–181.

Li J. X., Hu R. Z., Zhao C. H., Zhu J. J., Huang Y., Gao W., Li J. W. and Zhuo Y. Z. (2020a) Sulfur isotope and trace element compositions of pyrite determined by NanoSIMS and LA-ICP-MS: new constraints on the genesis of the Shuiyindong Carlin-like gold deposit in SW China. *Miner. Deposita* **55**, 1279–1298.

Li Z. X. and Li X. H. (2007) Formation of the 1300-km-wide intracontinental orogen and postorogenic magmatic province in Mesozoic South China: A flat-slab subduction model. *Geology* **35**, 179–182.

Li W. Y., Teng F. Z., Ke S., Rudnick R. L., Gao S., Wu F. Y. and Chappell B. W. (2010) Heterogeneous magnesium isotopic composition of the upper continental crust. *Geochim. Cosmochim. Acta* **74**, 6867–6884.

Li F. B., Teng F. Z., Chen J. T., Huang K. J., Wang S. J., Lang X. G., Ma H. R., Peng Y. B. and Shen B. (2016) Constraining ribbon rock dolomitization by Mg isotopes: Implications for the 'dolomite problem'. *Chem. Geol.* **445**, 208–220.

Li J. H., Wu P., Xie Z. J., Liu J. Z., Zhang S. J., Song W. F., Zhang B. Q., Li S. T., Xu L. Y. and Zheng L. L. (2021) Alteration and paragenesis of the basalt-hosted Au deposits, southwestern Guizhou Province, China: Implications for ore genesis and exploration. *Ore Geol. Rev.* **131** 104034.

Li W. Q., Zhao S. G., Wang X. M., Li S. L., Wang G. G., Yang T. and Jin Z. D. (2020b) Fingerprinting hydrothermal fluids in porphyry Cu deposits using K and Mg isotopes. *Sci. China: Earth Sci.* **63**, 108–120, in Chinese with English abstract.

Liang Q. L., Xie Z. J., Song X. Y., Wirth R., Xia Y. and Cline J. (2021) Evolution of invisible Au in arsenian pyrite in Carlin-type Au deposits. *Econ. Geol.* **116**, 515–526.

Liu J. Z., Li J. W., Zhou Z. G., Wang Z. P., Chen F. E., Qi L. S., Yang C. F., Hou L., Jin X. Y., Li J. H., Yang B. N., Xu L. Y., Zhang M., Zhang J. R., Tan L. J., Li S. T., Long C. X., Fu Z. K., He Y. N., Meng M. H. and Wang X. Y. (2017) New progress of exploration and research of Zhenfeng-Pu'an gold fully equipped exploration area. *Guizhou Geol.* **34**, 244–254, in Chinese with English abstract.

Liu S. A., Teng F. Z., He Y. S., Ke S. and Li S. G. (2010) Investigation of magnesium isotope fractionation during granite differentiation: Implication for Mg isotopic composition of the continental crust. *Earth Planet. Sci. Lett.* **297**, 646–654.

Liu J. Z., Wang Z. P., Yang C. F., Li J. H., Xie Z. J., Zheng L. L., Tan Q. P., Song W. F., Xu L. Y., Li S. T., Wang D. F., Chen F. E., Qing Y. J., Tan L. J. and Hu C. W. (2020) Multi-level structural detachment mineralization system of Carlin-type gold deposits in southern China. *China Sci. Technol. Achiev.* **21**, 49–51, in Chinese.

Liu J. M., Ye J., Liu J. J. and Gu X. X. (2001) Relationship between sediments-hosted micro-disseminated gold deposits and basin evolution: Case study in Youjiang Basin, South China. *Mineral Deposits* **20**, 367–377, in Chinese with English abstract.

Mercer C. N. (2021) Eocene magma plumbing system beneath Cortez Hills Carlin-type gold deposit, Nevada: Is there a deep-seated pluton? *Econ. Geol.* **116**, 501–513.

Muntean J. L. and Cline J. S. (2018) Diversity of Carlin-style gold deposits. *Rev. Econ. Geol.* **20**, 1–6.

Muntean J. L., Cline J. S., Simon A. C. and Longo A. A. (2011) Magmatic-hydrothermal origin of Nevada's Carlin-type gold deposits. *Nat. Geosci.* **4**, 122–127.

Peng Y., Shen B., Lang X. G., Huang K. J., Chen J. T., Yan Z., Tang W. B., Ke S., Ma H. R. and Li F. B. (2016) Constraining dolomitization by Mg isotopes: A case study from partially dolomitized limestones of the middle Cambrian Xuzhuang Formation, North China. *Geochem. Geophys. Geosyst.* **17**, 1109–1129.

Pi Q. H., Hu R. Z., Xiong B., Li Q. L. and Zhong R. C. (2017) In situ SIMS U-Pb dating of hydrothermal rutile: Reliable age for the Zhesang Carlin-type gold deposit in the golden triangle region. *SW China. Miner. Deposita* **52**, 1179–1190.

Qi L., Hu J. and Gregoire D. C. (2000) Determination of trace elements in granites by inductively coupled plasma mass spectrometry. *Talanta* **51**, 507–513.

Ressel M. W. and Henry C. D. (2006) Igneous geology of the Carlin trend, Nevada: Development of the eocene plutonic complex and significance for Carlin-type gold deposits. *Econ. Geol.* **101**, 347–383.

Su W. C., Heinrich C. A., Pettke T., Zhang X. C., Hu R. Z. and Xia B. (2009) Sediment-hosted gold deposits in Guizhou, China: Products of wall-rock sulfidation by deep crustal fluids. *Econ. Geol.* **104**, 73–93.

Su W. C., Zhang H. T., Hu R. Z., Ge X., Xia B., Chen Y. Y. and Zhu C. (2012) Mineralogy and geochemistry of gold-bearing arsenian pyrite from the Shuiyindong Carlin-type gold deposit, Guizhou, China: Implications for gold depositional processes. *Miner. Deposita* **47**, 653–662.

Su W. C., Dong W. D., Zhang X. C., Shen N. P., Hu R. Z., Hofstra A. H., Cheng L. Z., Xia Y. and Yang K. Y. (2018) Carlin-type gold deposits in the Dian-Qian-Gui "golden triangle" of Southwest China. *Rev. Econ. Geol.* **20**, 157–185.

Tan Q. P., Xia Y., Xie Z. J. and Yan J. (2015) Migration paths and precipitation mechanisms of ore-forming fluids at the Shuiyindong Carlin-type gold deposit, Guizhou. *China. Ore Geol. Rev.* **69**, 140–156.

Tan Q. P., Xia Y., Wang X. Q., Xie Z. J. and Wei D. T. (2017) Carbon-oxygen isotopes and rare earth elements as an exploration vector for Carlin-type gold deposits: A case study of the Shuiyindong gold deposit, Guizhou Province. *SW China. J. Asian Earth Sci.* **148**, 1–12.

Tang Q., Bao J., Dang Y., Ke S., Zhao Y. J. E. and Letters P. S. (2018) Mg-Sr-Nd isotopic constraints on the genesis of the giant

Jinchuan Ni-Cu-(PGE) sulfide deposit. *NW China. Earth Planet. Sci. Lett.* **502**, 221–230.

Teng F. Z. (2017) Magnesium Isotope Geochemistry. *Rev. Mineral. Geochem.* **82**, 219–287.

Teng F. Z., Li W. Y., Ke S., Marty B., Dauphas N., Huang S., Wu F. Y. and Pourmand A. (2010) Magnesium isotopic composition of the Earth and chondrites. *Geochim. Cosmochim. Acta* **74**, 4150–4166.

Tipper E. T., Galy A. and Bickle M. J. (2006) Riverine evidence for a fractionated reservoir of Ca and Mg on the continents: Implications for the oceanic Ca cycle. *Earth Planet. Sci. Lett.* **247**, 267–279.

Tipper E. T., Calmels D., Gaillardet J., Louvat P., Capmas F. and Dubacq B. (2012) Positive correlation between Li and Mg isotope ratios in the river waters of the Mackenzie Basin challenges the interpretation of apparent isotopic fractionation during weathering. *Earth Planet. Sci. Lett.* **333–334**, 35–45.

Vaughan J. R., Hickey K. A. and Barker S. L. L. (2016) Isotopic, chemical, and textural evidence for pervasive calcite dissolution and precipitation accompanying hydrothermal fluid flow in low-temperature, carbonate-hosted, gold systems. *Econ. Geol.* **111**, 1127–1157.

Wang G. Z., Hu R. Z., Su W. C. and Zhu L. M. (2002) Basin fluid migration and mineralization of Youjiang Basin, Dian-Qian-Gui area. *Science in China (Series D)* **32**, 78–86, in Chinese with English abstract.

Wang S. J., Teng F. Z., Li S. G. and Hong J. A. (2014) Magnesium isotopic systematics of mafic rocks during continental subduction. *Geochim. Cosmochim. Acta* **143**, 34–48.

Wang S. J., Teng F. Z. and Scott J. M. (2016) Tracing the origin of continental HIMU-like intraplate volcanism using magnesium isotope systematic. *Geochim. Cosmochim. Acta* **185**, 78–87.

Xie Z. J., Xia Y., Cline J. S., Yan B. W., Wang Z. P., Tan Q. P. and Wei D. T. (2017) Comparison of the native antimony-bearing Paiting gold deposit, Guizhou Province, China, with Carlin-type gold deposits, Nevada, USA. *Miner. Deposita* **52**, 69–84.

Xie Z. J., Xia Y., Cline J. S., Koenig A., Wei D. T., Tan Q. P. and Wang Z. P. (2018a) Are there Carlin-type Au deposits in China? A comparison between the Guizhou China and Nevada USA deposits. *Rev. Econ. Geol.* **20**, 187–233.

Xie Z. J., Xia Y., Cline J. S., Pribil M. J., Koenig A., Tan Q. P., Wei D. T., Wang Z. P. and Yan J. (2018b) Magmatic origin for sediment-hosted Au deposits, Guizhou Province, China: In situ chemistry and sulfur isotope composition of pyrites, Shuiyindong and Jinfeng deposits. *Econ. Geol.* **113**, 1627–1652.

Yin R. S., Deng C. Z., Lehmann B., Sun G. Y., Lepak R. F., Hurley J. P., Zhao C. H., Xu G. W., Tan Q. P., Xie Z. J. and Hu R. Z. (2019) Magmatic-hydrothermal origin of mercury in Carlin-style and epithermal gold deposits in China: Evidence from mercury stable isotopes. *ACS Earth Space Chem.* **3**, 1631–1639.

Young E. D. and Galy A. (2004) The isotope geochemistry and cosmochemistry of magnesium. *Rev. Mineral. Geochem.* **55**, 197–230.

Zaw K., Meffre S., Lai C. K., Burrett C., Santosh M., Graham I., Manaka T., Salam A. and Kamvong T. (2014) Tectonics and metallogeny of mainland Southeast Asia-A review and contribution. *Gondwana Res.* **26**, 5–30.

Zhang Q., Bai J. F. and Wang Y. (2012) Analytical scheme and quality monitoring system for China Geochemical Baselines. *Earth Sci. Front.* **19**, 33–42, in Chinese with English abstract.

Zhu J., Zhang Z. C., Santosh M. and Jin Z. L. (2020) Carlin-style gold province linked to the extinct Emeishan plume. *Earth Planet. Sci. Lett.*, 115940.

Zhu J. J., Zhong H., Xie G. Q., Zhao C. H., Xu L. L. and Lu G. (2016) Origin and geological implication of the inherited zircon from felsic dykes, Youjiang basin. *Chian. Acta Petrol. Sin.* **32**, 3269–3280, in Chinese with English abstract.

Associate editor: Adam Simon